Acta Materialia 279 (2024) 120267

Contents lists available at ScienceDirect

Acta Materialia

journal homepage: www.elsevier.com/locate/actamat

Full length article

Operando study of the dynamic evolution of multiple Fe-rich intermetallics of an Al recycled alloy in solidification by synchrotron X-ray and machine learning

Kang Xiang [a], Ling Qin [a,b], Yuliang Zhao [a,c], Shi Huang [a], Wenjia Du [a,d], Elodie Boller [e], Alexander Rack [e], Mengnie Li [f,*], Jiawei Mi [a,g,*]

[a] School of Engineering, University of Hull, Hull, HU6 7RX, UK
[b] Centre of Innovation for Flow Through Porous Media, Department of Petroleum Engineering, University of Wyoming, Laramie, WY 82071, USA
[c] Neutron Scattering Technical Engineering Research Centre, School of Mechanical Engineering, Dongguan University of Technology, Dongguan, 523808, PR China
[d] Department of Engineering Science, University of Oxford, Oxford OX1 3PJ, UK
[e] ESRF - The European Synchrotron Radiation Facility, 71 Avenue des Martyrs, 38000 Grenoble, France
[f] Faculty of Materials Science and Engineering, Kunming University of Science and Technology, Kunming, 650093, PR China
[g] School of Materials Science and Engineering, Shanghai Jiao Tong University, Shanghai, 200240, PR China

ARTICLE INFO

Keywords:
Synchrotron X-rays
Diffraction
Tomography
Fe-rich intermetallics
Recycled Al alloys
Ultrasound melt processing
Solidification
Multiphysics modelling

ABSTRACT

Using synchrotron X-ray diffraction, tomography and machine-learning enabled phase segmentation strategy, we have studied under operando conditions the nucleation, co-growth and dynamic interplays among the dendritic and multiple intermetallic phases of a typical recycled Al alloy (Al5Cu1.5Fe1Si, wt.%) in solidification with and without ultrasound. The research has revealed and elucidated the underlying mechanisms that drive the formation of the very complex and convoluted Fe-rich phases with rhombic dodecahedron and 3D skeleton networks (the so-called Chinese-script type morphology). Through statistical microstructural analyses and numerical modelling of the ultrasound melt processing, the research has demonstrated that a short period of ultrasound processing of just 7 s in the liquid state is able to reduce the average size of the α-Al dendrites and the Fe-containing intermetallic phases by ~5 times compared to the cases without ultrasound. For the first time, this work has revealed fully the nucleation and growth dynamics of the convoluted morphology of the Fe-containing intermetallic phases in 4D domain. The research has also demonstrated clearly the beneficial effects of applying ultrasound to control the Fe phases' morphology in recycled Al alloys and it is one of the most effective and green processing strategies.

1. Introduction

Globally, the current annual demand for primary aluminium (Al) is estimated at ~70 million tons [1]. Compared to the production of primary Al, the uses of secondary Al or recycled Al consume only ~7% of the energy [2-5]. Hence, it is vital to maximise the reuses and recycling rate of secondary Al in order to reduce the greenhouse gas emissions in Al industry. Dependent on the alloy systems and/or manufacturing routes (i.e., casting or solid state forming), some of the beneficial alloying elements in one Al alloy may become the detrimental elements in other alloys. For example, Fe is the most common detrimental element in almost all commercial Al alloys, which is often accumulated in the sorting and remelting processes. For the most Al-Cu alloys, Si is another impurity element. The upper limit of Fe and Si content in industrial primary Al-Cu alloys is normally controlled at below 0.15 wt% and 0.1 wt% respectively [6-8]. When excessive amount of Fe and Si are present in Al-Cu alloys, different type of brittle Fe-rich intermetallic phases, e.g., $Al_3(CuFe)$, $Al_6(CuFe)$, β-Al_7Cu_2Fe (β-Fe) and α-$Al_{15}Fe_3(SiCu)_2$ (α-Fe) [9-13] will form and grow into needle-shaped, plate-shaped or complex-shaped morphologies [12-14] as typically illustrated in Fig. 1 (in a 2-dimensional sectional view). These Fe phases often cause strain incompatibility at their interface with the surrounding Al matrix, initiating cracks that propagate along the interface at much lower level of stresses, damaging greatly the castability and mechanical properties of the alloys [10,15].

Therefore, to maximise the recycling or re-uses of Al based materials

* Corresponding authors.
E-mail addresses: limengnie@kust.edu.cn (M. Li), J.Mi@hull.ac.uk (J. Mi).

https://doi.org/10.1016/j.actamat.2024.120267
Received 14 May 2024; Received in revised form 24 July 2024; Accepted 3 August 2024
Available online 5 August 2024

with higher Fe concentration in a net-zero emission society in the near future, it is critical to develop efficient and effective methodologies to restrict the detrimental Fe phases or to modify/change the damaging phase morphology into beneficial ones in order to improve the mechanical properties. At present, the most common approach to tailor and/or modify these Fe phases is by adding neutralization elements (e.g., Mn and Cr [14,16,17]) or applying physical external fields (ultrasonic or magnetic fields [18-22]) to control their nucleation and growth dynamics with the aims of achieving the desired final size, morphology, and distribution. Ultrasonic melt processing (USMP) has been long recognised as an efficient and environment-friendly method for degassing, structure refinement and chemistry homogenisation [18-21]. Recently, extensive research [23-31] has been carried out to study the effect of USMP on the microstructures of intermetallics in numerous Al alloys. For example, Kotadia et al. [28] reported that USMP could convert the coarse Chinese-script α-$Al_{15}(Fe, Mn)_3Si_2$ phases into refined polygonal morphology in Al-2Si-2Mg-1.2Fe-(0.5,1.0)Mn alloys. Barbosa et al. [30] also found that USMP could promote the formation of α-$Al_{17}(Fe_{3.2}, Mn_{0.8})Si_2$ and α-Al_8Fe_2Si phases, and suppress the formation of plate-shaped β-Al_5FeSi phases in the Al-9.2Si-2.3Cu-0.7Fe alloy. However, most of previous research has used conventional ex-situ microstructural characterisation techniques to analyse the post-solidified microstructures [32]. Unfortunately, in such structures, the highly transient phenomena occurring at the phase nucleation stage or phase transformation/growth at different temperatures are already missed or obscured [33-35]. Hence, the dynamic structural evolution from the onset of Fe phase nucleation to a fully developed complex 3-dimensional (3D) morphology have not been fully understood or quantified.

In the past 25 years, the 3rd generation synchrotron X-ray sources (especially the extremely brilliant source at the European Synchrotron Radiation Facility, ESRF – the first 4th generation synchrotron X-ray source) have provided materials scientists and engineers with the powerful X-ray beams and relevant *in-situ* instruments for studying in real-time the growth dynamics of different intermetallic phases in metal alloys [33,36-50]. For example, in 2012, Kim et al. [35] studied, by using radiography, the solidification sequences of the Fe phases in the Al-9.5Si-3Cu-(1.2, 4.2)Fe alloys. In 2014, Pencreobutr et al. [51] used tomography to confirm that the plate-shaped β-Al_5FeSi phases were nucleated on or near the oxide inclusions or the Al dendrites in the Al-7.5Si-3.5Cu-0.6Fe alloy. Later in 2020 and 2021, Feng et al. and Song et al. [34,52,53] used X-ray radiography and tomography to reveal again that majority of the Al_3Fe phases in the hypereutectic Al-Fe alloys were indeed nucleated near the surface oxides. Their growth into different morphologies were controlled mainly by the intrinsic crystallography (i.e., twinning) [34,52].

However, most of these *in-situ* experiments were focused on studying the faceted growth dynamics of some Fe phases of simple alloy composition (e.g., plate-shaped Al_3Fe and β-Fe phases) [34,51-56]. So far, to the best of the authors' knowledge, there have been very limited research on studying, *in-situ* and in operando conditions, the nucleation and growth dynamics of the convoluted 3D Chinese-script type Fe phases. The dynamic interplay between the primary Al dendrites, the Chinese-script Fe phases and other types of Fe phases as well as their co-growth in the solidification process are the fundamental driving forces for producing such complex and convoluted 3D Fe intermetallic phases. Unfortunately, in this aspect, systematic and real-time studies carried out under operando conditions have not been reported yet. Hence, the nucleation and growth dynamics of the convoluted structures of the Chinese-script type Fe intermetallic phases in four dimensional domains (3D space + time) have not been fully understood. Here, we present our recent operando research work of using the fast synchrotron X-ray tomography available at beamline ID19 of the ESRF plus machine-learning assisted phase segmentation techniques to tackle the challenging scientific issue. Our work reveals the 3D nucleation dynamics of the Fe phases in a typical multiple-component recycled Al-Cu alloy (Al5Cu1.5Fe1Si, wt.%); and how co-growth of the multiple Fe phases lead to the formation of the complex and convoluted 3D Chinese-script phases. In addition, the beneficial effects of applying ultrasound to control the primary Al dendrites and to alter the Fe phase growth dynamics as well as the final 3D morphology were also quantified and elucidated in this work. Because of the page constraint, the results concerning the effects of different type Fe-rich intermetallics (including morphology) on the mechanical properties will be reported later in a separate paper.

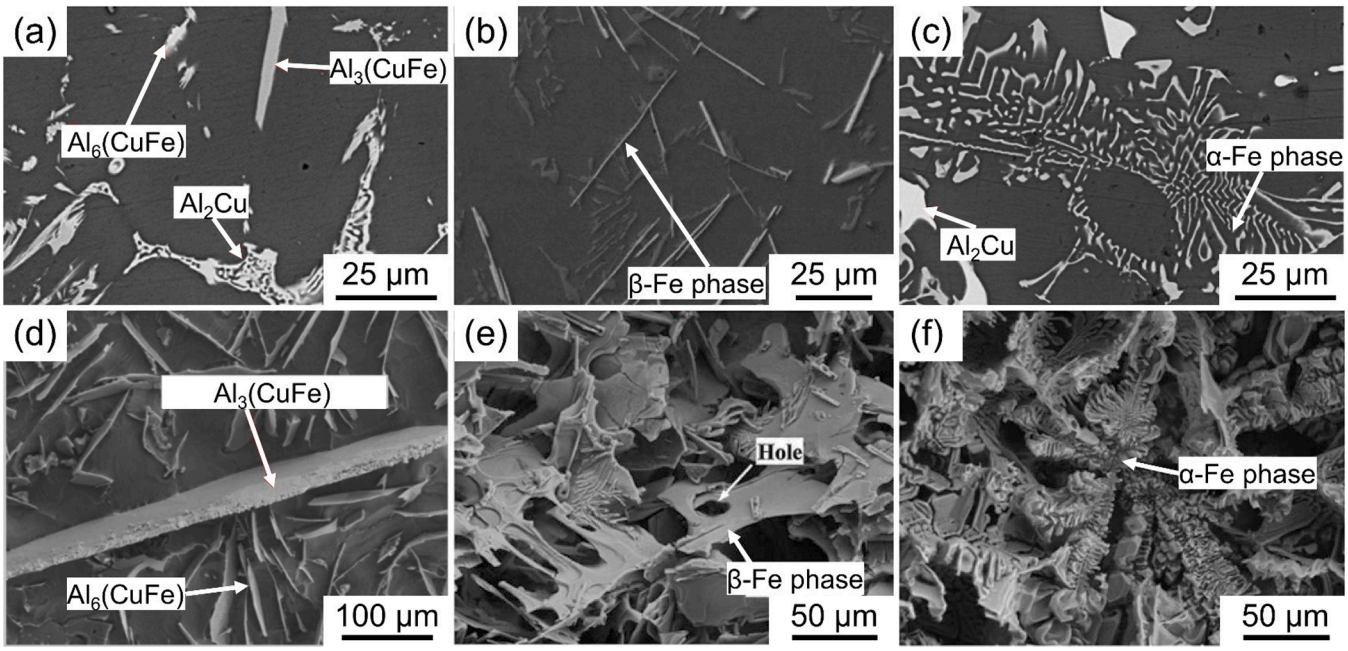

Fig. 1. Scanning electron microscopy (SEM) images of the typical Fe-rich intermetallics in recycled Al-Cu alloys. (a) rod-shaped $Al_3(CuFe)$ and $Al_6(CuFe)$ phases. (b) plate-shaped β-Fe phases. (c) Chinese-script type α-Fe phases. (d)-(f) The corresponding deeply-etched images [12-14].

2. Experiments and methods

2.1. Alloys and samples

The Al5Cu1.5Fe1Si alloy (a total weight of ~500 g) was made by melting 462.5 g pure Al (99.9 %), 25 g pure Cu (99.99 %), 7.5 g pure Fe (99.99 %), and 5 g pure Si (99.99 %) (purchased from Goodfellow, UK) in an alumina crucible (the crucible inner surface was coated with a boron nitride spray). The Al melt was held at 900 °C for 2 h to allow the Fe and Si to be dissolved completely into the Al melt and the composition homogenised. Then the alloy melt temperature was decreased to ~720 °C before vacuum-sucked into a quartz tube (Φ 2 × 10 mm) by using a dedicated counter-gravity casting apparatus [57] to form the round bar samples.

2.2. Experimental apparatus and synchrotron X-ray parameters

The operando solidification plus synchrotron X-ray tomography experiments were carried out at the beamline ID19 of the ESRF, and Fig. 2 shows the experimental apparatus and setup. The apparatus consists of 3 parts: (1) an ultrasound generator (Hielscher UP100H, 30 kHz with adjustable amplitude setting from 20 to 100 %) and a custom-made Nb sonotrode (2 mm diameter tip, 74 mm long), (2) two small electrical resistance furnaces (a top and a bottom furnace), and (3) a special dumbbell-shaped quartz tube sample holder.

This sample holder has a narrow section (2 mm inner diameter) in the middle where X-ray can pass through with sufficient flux for tomography acquisition. The top and bottom bigger-diameter sections (Φ 10 mm ID) are designed for accommodating the metal alloy.

Before any in-situ tomography experiments, melting of the alloy sample and control of the melt temperature of each sample were thoroughly tested and repeated to ensure a consistent operation and repeatable thermal profile for all subsequent tomography acquisitions. The temperature control and calibration procedure are shown in Fig. S1 of the Supplementary Materials. Three K-type thermocouples (labelled TC1, TC2 and TC3 in Fig. 2) were used to monitor and record the temperatures of the top furnace, the alloy melt, and the bottom furnace (during testing and calibration, TC2 was inserted into the melt, but it was lifted out of the melt during tomography acquisition). After 6 times of thoroughly testing and iteratively refining the temperature control programs for both furnaces, a consistent and repeatable cooling profile (see Fig. S1) was achieved as described in Section 1 of the Supplementary Materials. Then this program was used for all the subsequent experiments. The cooling rate of the melt was set at 0.5 °C/s. For the alloy with USMP, ultrasound setting of 100 % (equivalent to the peak-to-peak amplitude of 96 μm [58]) was used to apply 7 s of ultrasound into the melt when the alloy melt reached to 635 °C. Immediately prior to the tomography acquisition, the thermocouple (TC2) was lifted out of the melt.

A pink X-ray beam of 26 keV and a CMOS camera (type: pco.dimax, Excelitas, Germany) were used in the tomography acquisition. The field of view (FOV) was 1008 × 1008 pixels with an effective pixel size of 1.1 μm via a 10 × optical microscope. 1000 projections (each with an exposure time of 2.0 ms) were taken over 180° of sample rotation. Therefore, the total time required for each tomographic scan was about ~2 s. After one tomography scan completed, the sample continued to rotate for 3.5 × 360° before taking the next tomography scan. Hence, the time interval between two consecutive tomography scans was 14 s. Table 1 lists the parameters used.

To determine experimentally the phases of the alloy to appear in the solidification process (without the application of ultrasound), synchrotron X-ray diffraction was also used to characterise the phase formation sequences in real-time at beamline I12 of the Diamond Light Source (DLS), UK. A monochromatic X-ray of 100.03 KeV (wavelength of 0.1236 Å) and a 2D flat-panel detector (Pilatus3 X CdTe 2 M, 1475 × 1679 pixels with the pixel size of 172 × 172 μm^2) were used for acquiring the diffraction patterns. The sample-to-detector distance was set at 408.02 mm.

Table 1
The parameters used for the tomography acquisition at ID19, ESRF.

X-ray Beam	26 keV (pink)
Scintillator	LuAG: Ce 25 μm
Detector	pco.dimax
Effective pixel size	1.1 μm
Field of view (FOV)	1008 × 1008 pixels
Exposure time	2.0 ms
Optical magnification	10 ×
No. of projection	1000
Sample-to-scintillator distance	300 mm (phase contrast)

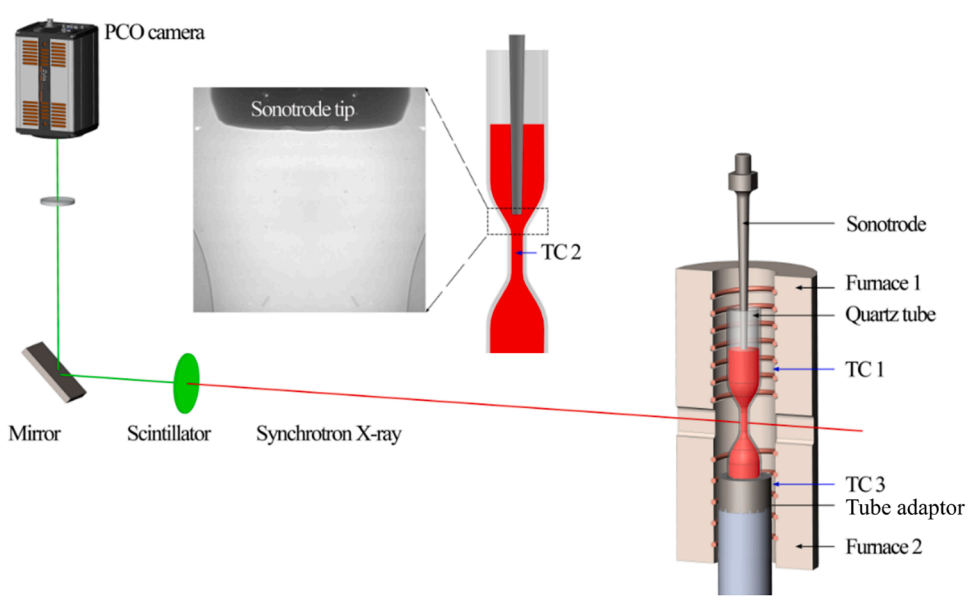

Fig. 2. A schematic, showing the experimental setup and the special quartz sample holder for the synchrotron X-ray tomography experiments at ID19 of the ESRF.

2.3. Machine-learning enabled tomography data processing and phase segmentation

The tomography data was reconstructed using the standard filtered-back projection PyHST2 software package, which has been highly optimised for speed and data throughput using the ESRF-specific computing infrastructure [59]. The image preprocessing and 3D reconstruction were achieved by ImageJ (1.52a, NIH, USA) [60] and Avizo 3D (2021.1, Thermo Fisher Scientific, USA) respectively. The Trainable Weka Segmentation Plugin [61] in ImageJ software was then used for the dataset phase segmentation. The plugin combines a set of machine learning algorithms to perform pixel-based segmentations.

Fig. S4 shows schematically the machine-learning assisted tomography data processing procedure. Firstly, a number of image filters (Gaussian blur, Hessian, Membrane projections, Sobel filter, and Difference Gaussians) available in ImageJ were used to extract the image features from reconstructed tomographic 2D slices. Secondly, a set of pixel clusters were purposely defined and labelled. Thirdly, a WEKA algorithm with the default classifier (FastRandomForest) was automatically applied to separate these pixel clusters [61]. Users can also provide sensible inputs at each iteration by correcting or adding new clusters [41]. Finally, the well-trained dataset would be used in segmenting the remaining tomographic data. Figs. S5 & 6 illustrate the difference between the raw images and machine-learning processed images. Clearly the accuracy of phase identification and the efficiency of phase segmentation have been greatly enhanced by the machine learning method.

From the different phases' X-ray absorption contrast only, it is very challenging to precisely identify the different Fe-containing phases (e.g., to differentiate the Al_3Fe, from the $Al_{15}Fe_3(SiCu)_2$ or the Al_7Cu_2Fe). Here, we combined *in-situ* diffraction and computational phase diagram calculation to accurately identify the multiple-Fe phases during the cooling process. Eventually, eight different classes of well-defined features i.e., Al_3Fe, α-Fe nucleus, α-Fe skeleton, α-Fe colony, β-Fe, α-Al, liquid melt, and pores were classified and segmented. The processed datasets were further rendered and visualised by using Avizo. After reconstructing the 3D morphologies of different phases, the statistical data concerning their size and spatial distribution [62] were directly extracted from ImageJ and Avizo 3D.

3. Results

3.1. Formation sequences of the multiphases quantified by in-situ X-ray diffraction and phase diagram calculation

Fig. 3a shows the crystalline phases reactions and transitions of the alloy, calculated by JMatPro ® (v13.2) using the Scheil-Gulliver model [63]. Fig. 3b and Video 1 shows the synchrotron X-ray diffraction intensity spectra during solidification without ultrasound (from 750 to 300 °C). Fig. 3c highlights the diffraction patterns from 630 to 500 °C, and Fig. 3d enlarges again the dotted-box region in Fig. 3c.

Clearly, the first crystalline diffraction peak appeared at $2\theta = 4.95°$ and 628.4 °C. This peak is indexed as α-Al and Al_3Fe. The Bragg peaks of the two phases are very close and therefore the experimentally measured peaks overlapped. JMatPro phase calculation indicated that the α-Al appeared first at ~ 632 °C (see Fig. 3a). When temperature reached 615.6 °C, the peaks at $2\theta = 3.55°$ appeared and it is indexed as $Al_{15}Fe_3(SiCu)_2$ (named α-Fe phase hereafter). When the melt was further cooled down to 565.3 °C, the peak near $2\theta = 3.1°$ appeared and this is the Al_7Cu_2Fe phase (named β-Fe phase hereafter). As the melt was

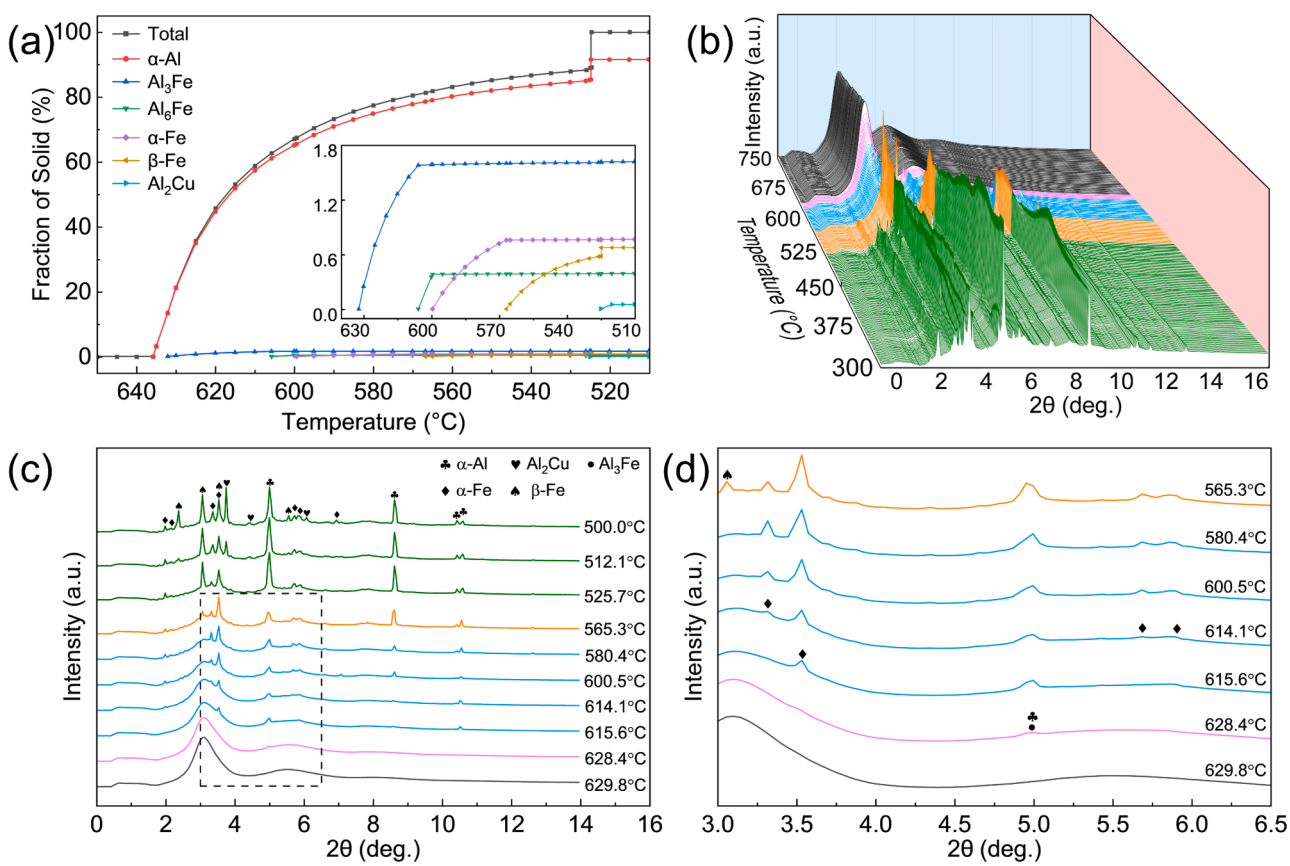

Fig. 3. (a) Phase transition sequence of the Al5Cu1.5Fe1Si alloy during solidification calculated by JMatPro® using the Scheil-Gulliver model. (b) The *in-situ* synchrotron X-ray diffraction intensity water-fall plot (Please also see Video 1). (c) The diffraction spectra extracted from (b), highlighting those from 630 to 500 °C. (d) The spectra inside the dotted-box region in (c) are enlarged again to show more clearly the appearance of the different phases.

cooled to 525.7 °C, a sharp peak near 2θ = 3.75° appeared, indicating the formation of the Al_2Cu phase. Then, the diffraction patterns remained in similar profiles until 300 °C (despite a slightly increase in intensity). Hence, the fully solidified sample consists of α-Al, Al_3Fe, α-Fe, β-Fe and Al_2Cu phases.

Comparing the *in-situ* diffraction results with the JMatPro calculations, we found that there was no Al_6Fe phase detected in the measured diffraction spectra, indicating that a slight non-equilibrium phase transition occurred during solidification. The Al_6Fe phase is a typical metastable phase and need sufficient time for the transformation to occur in a narrow temperature range (i.e., 605–600 °C).

3.2. Dynamic morphology evolution of the multiphases revealed by in-situ X-ray tomography and machine-learning enabled phase segmentation

The synchrotron X-ray tomography data collected in operando allow us to reveal in real-time the multiphases dynamic morphology evolution in the solidification process. Figs. 4 and 5 show the machine learning segmented and reconstructed 2D tomographic slices at some critical temperatures for this alloy without and with USMP. Such systematic and accurate segmentation of the different phases allow us to track and study the nucleation and growth dynamics of the different phases. Our focus is on the complex Fe-rich intermetallics as well as their interplays with the primary α-Al dendrites. To avoid the convoluted effects of the Al_2Cu phases formed in the final stage, all tomography data presented here are those prior to the formation of the Al_2Cu (i.e., above 525 °C).

Fig. 4a and Video 2 show a typical scenario when sufficient number of the primary α-Al dendrites and Fe-intermetallic phases appeared in the FOV at ~615 °C. The Fe phases have sufficient number of polygonal nuclei and skeleton branches for sensible statistical analyses. As solidification proceeded, the primary α-Al dendrites continued to grow with the primary and secondary dendritic arms gradually coarsened. Many needle-shaped β-Fe phases were also formed in the vicinity of the residual melt when the temperature cooled to ~565 °C. These β-Fe phases grew laterally into plate-shaped morphology, wrapping around and between the α-Al dendrites. In the case with the USMP, Fig. 5a and Video 3 show that the α-Al dendrites were considerably refined, and the α-Fe phases became more compact after USMP.

3.2.1. α-Al phase morphology evolution and the effect of USMP

Fig. 6 shows the primary α-Al dendrites of the alloy during solidification without USMP and with USMP when sufficient number of α-Al dendrites appeared in the FoV. The size of the α-Al dendrites is extracted from the typical tomographic volume. In the case without USMP, the α-Al dendrites had primary dendrite arms of ~250 μm long and an average size of 5.6×10^3 μm^2. While in the USMP case, the primary dendrite arms were reduced to ~120 μm long with an average size of 1.1×10^3 μm^2 after just 7 s of USMP.

3.2.2. Spatial relationships between the α-Al dendrites and multiple Fe phases

Figs. 7a shows that different Fe phases were formed in the interdendritic region during solidification without USMP (Video 2 shows more vividly the machine-learning segmented phases as compared to the original tomography data). Fig. 7b and Video 3 show the case with USMP. The size and distribution of Fe phases in the USMP case became more homogeneous compared to those without USMP. The statistical results reveal that, without USMP, ~20 % Fe phases were near-spherical

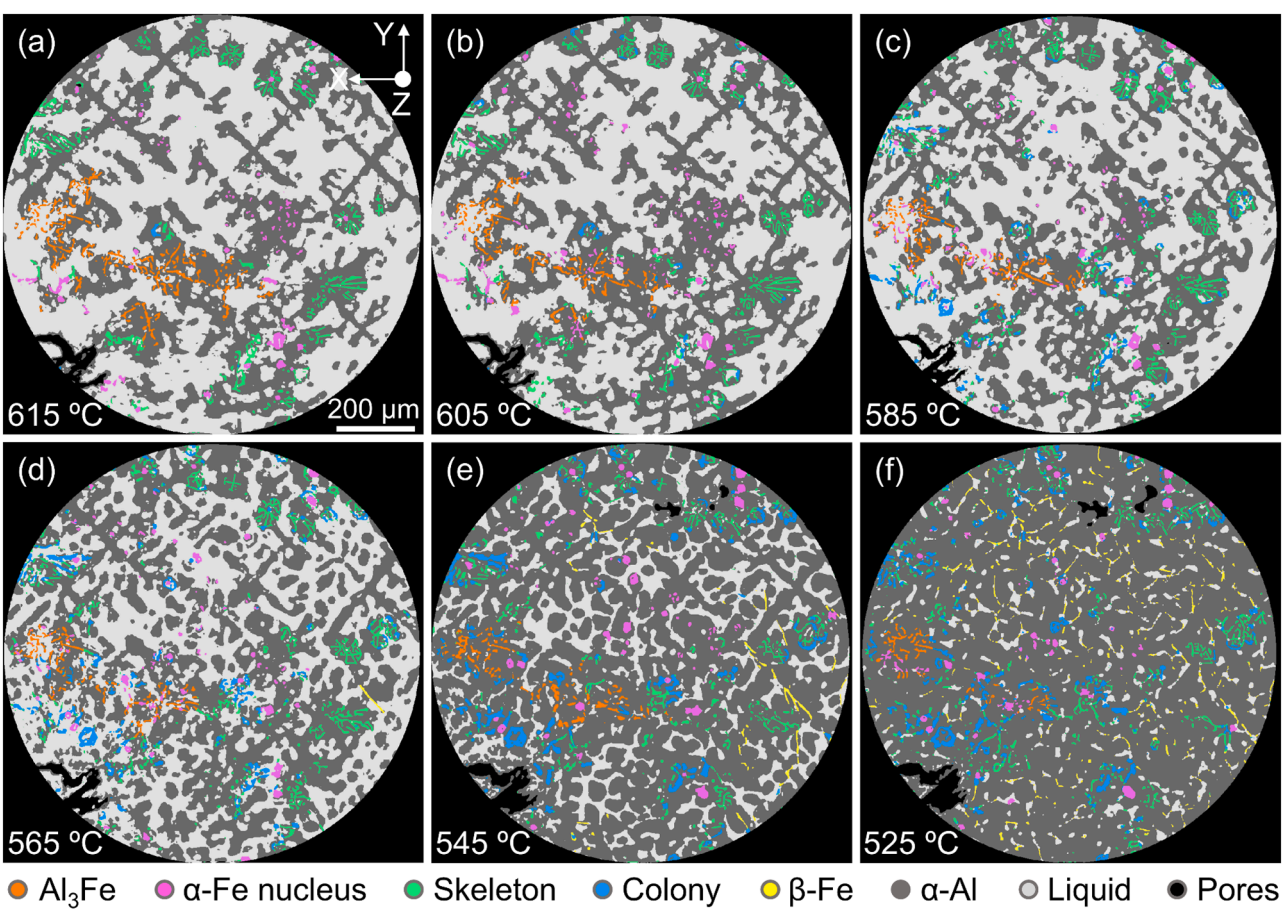

Fig. 4. Typical machine-learning processed tomographic slices (No. 640 of the 1000 projections) of the Al5Cu1.5Fe1Si alloy at some critical temperatures in solidification without USMP.

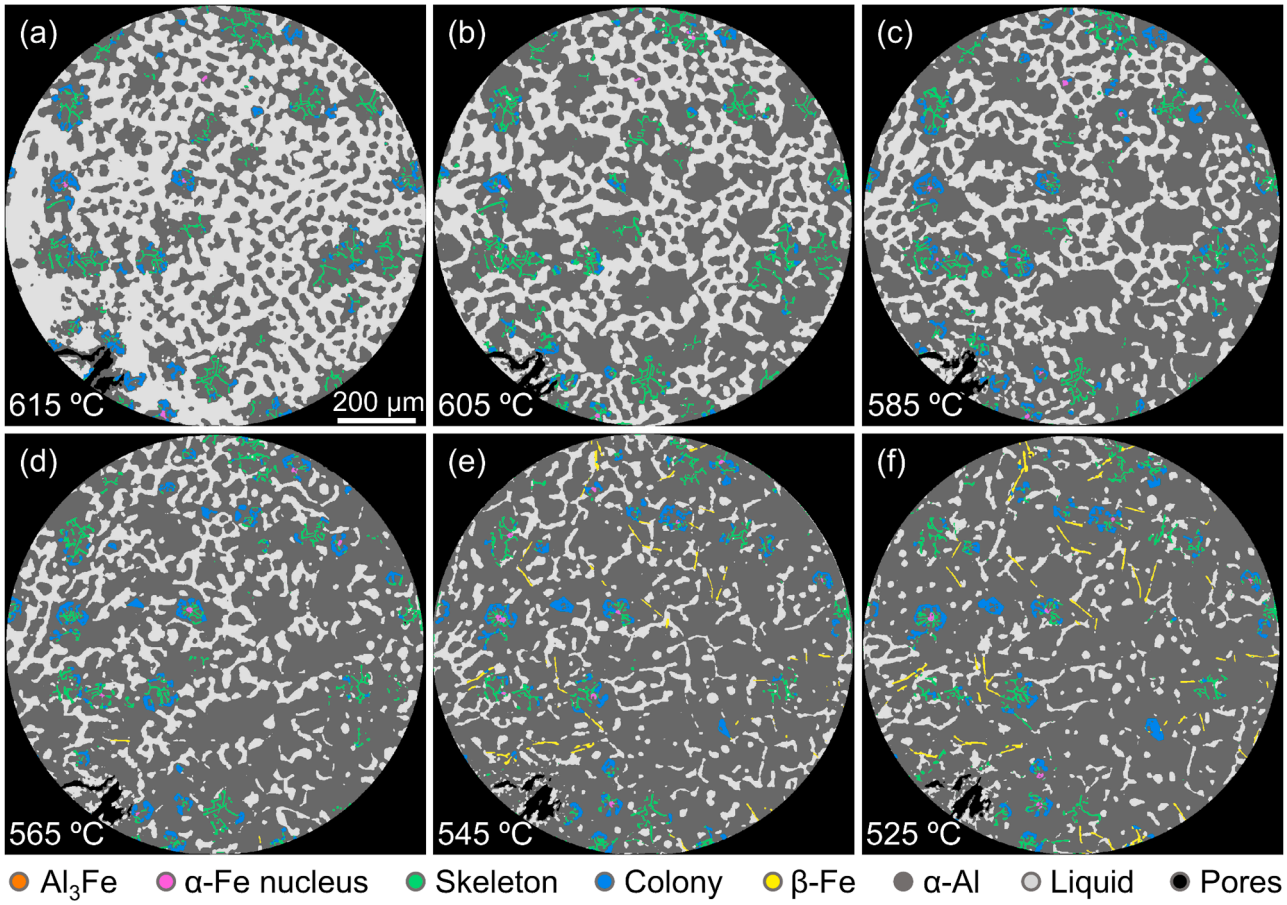

Fig. 5. Typical machine-learning processed tomographic slices (at the same number of projections) of the Al5Cu1.5Fe1Sialloy at the critical temperatures in solidification with USMP.

or polygonal nuclei (i.e., particles smaller than 5×10^3 μm^3), while ~50 % Fe phases grew into large clusters with an average size reaching 2.0×10^5 μm^3. In the USMP case, the number of Fe phase clusters was reduced to ~15 % and most of them were smaller colonies with an average size of 4.2×10^4 um^3. Furthermore, for the case without USMP, the interdendritic region spread from 10 to 60 μm. For the USMP case, it concentrated in the 20 - 30 μm region (Fig. 7f), resulting in much smaller free space for the Fe phases to grow, hence a smaller and more compact structure.

3.2.3. Co-growth dynamics of the multiple Fe-rich intermetallics in solidification

Several typical Fe phases are extracted to illustrate the evolution of their morphology. Fig. 8a shows a cluster of irregular Al_3Fe phases (without USMP) formed due to the initial segregation of Fe element in the melt. As the temperature decreased, α-Fe phases started to nucleate either directly from the melt or by from the Al_3Fe phases (some of the Al_3Fe phases acted as the nucleation sites for the α-Fe phases), and then gradually evolved into polygonal structures. Interestingly, some of the polygonal structures appeared as a near prefect rhombic dodecahedron in 3D space (Figs. 8b1&2 and Video 4). Subsequently, skeleton branches grew epitaxially along the tips or edges of the nucleus to form hopper-shaped structures. As the growth proceeded, the skeleton structures gradually closed up, forming α-Fe colonies in 3D space.

Similarly, this evolution was observed for the α-Fe colonies in the alloy with USMP (Figs. 9a1-5). The main difference is that these colonies were more compact, and the growth was completed at early stages (remained the same size in the subsequent solidification process). As the solidification proceeded, several plate-shaped β-Fe phases were observed to form from the residual melts without and with USMP (Figs. 8c and 9b and Video 5). These β-Fe phases were found to nucleate from the residual liquid melt rather than from the nearby α-Fe phases. These β-Fe phases then grew laterally and branched out, wrapping around the dendrite arms, and eventually impinging on each other or the nearby α-Fe phases, which is consistent with the observation in other Al alloy systems [35,51,55,56,64].

3.3. Modelling and simulation of the acoustic pressure, melt flow and temperature fields

To obtain more quantitative information about the effects of USMP on the liquid melt, we have simulated the ultrasonic pressure fields, the temperature evolution of the melt and the resulting melt velocity fields during USMP and afterwards (after the USMP was completed). Fig. 10a shows the computational domain (the same as the experimental geometry in Fig. 2), the mesh structures and boundary conditions. The governing equations, numerical computing methods and thermophysical properties employed in the simulation are described in Sections 4 - 7 of the Supplementary Materials.

To validate the simulation results, the measured temperature profile was compared with the simulated profile (see Fig. 10b for the temperature profile measured at P2) and they matched very well. Fig. 10c & d show the simulated pressure field and fluid flow velocity field at P1 (0.5 mm below the sonotrode tip) and P2 (the centre of the X-ray images) during USMP and afterwards. Figs. 10e & f depicts the time-evolved evolution of the pressure field and melt velocity vector maps

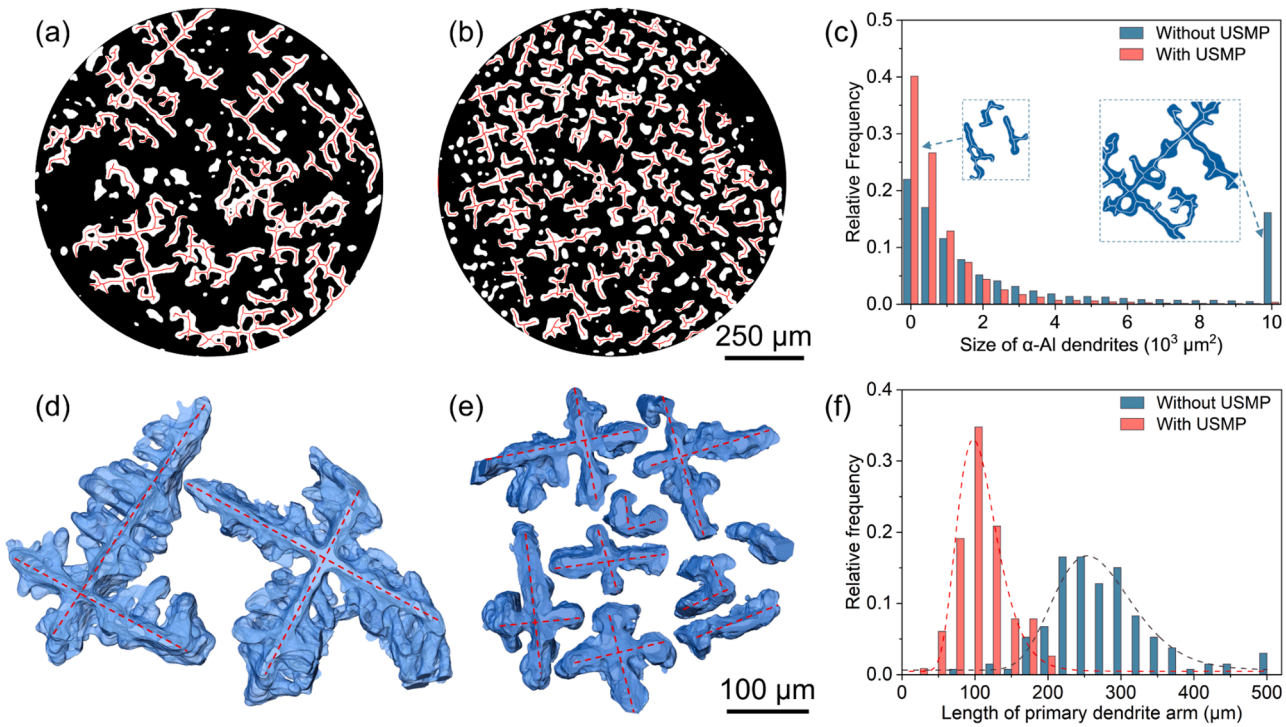

Fig. 6. (a) The typical tomographic slices (a binarized image with the red lines delineating the skeleton of the dendrites), showing the distribution of the primary α-Al dendrites in the alloy without USMP (Video 2 shows more vividly the machine-learning segmented α-Al dendrites). (b) shows the case with USMP (also see Video 3). (c) size distribution of the primary α-Al dendrites for both cases. (d) and (e) The typical 3D α-Al dendrites (The Fe phases, melt, and pores are removed to highlight the dendrite morphology). (f) Distribution of the primary dendrite arms for both cases.

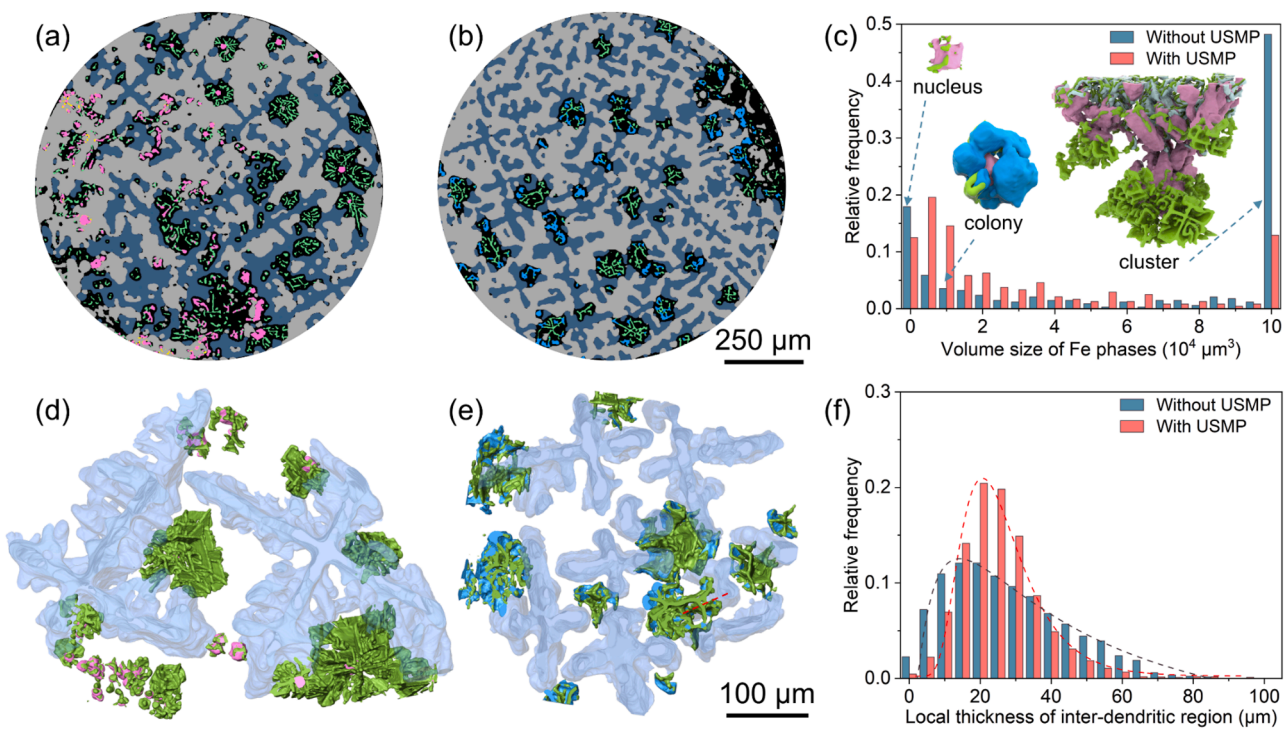

Fig. 7. (a) The typical slices, showing the distribution of the Fe phases in the alloy without USMP (Video 2 shows more vividly the machine-learning segmented Fe phases). (b) the case with USMP (also see Video 3). (c) The size distribution of the Fe phases for both cases. (d) and (e) Spatial relationships between the α-Al dendrites and Fe phases in 3D space. (f) Local thickness of the inter-dendritic region for both cases.

in the sampled area in approximately one half of an ultrasound cycle. It is clear that the ultrasonic pressures inside the melt followed the induced pressure wave pattern, oscillating cyclically in the range of ±1.5 MPa, which produced oscillating velocity fields at P1 (the maximum value of 180 mm/s) and P2 (the maximum value of 155 mm/s) during USMP. Immediately after USMP, the pressure and velocity very quickly damped

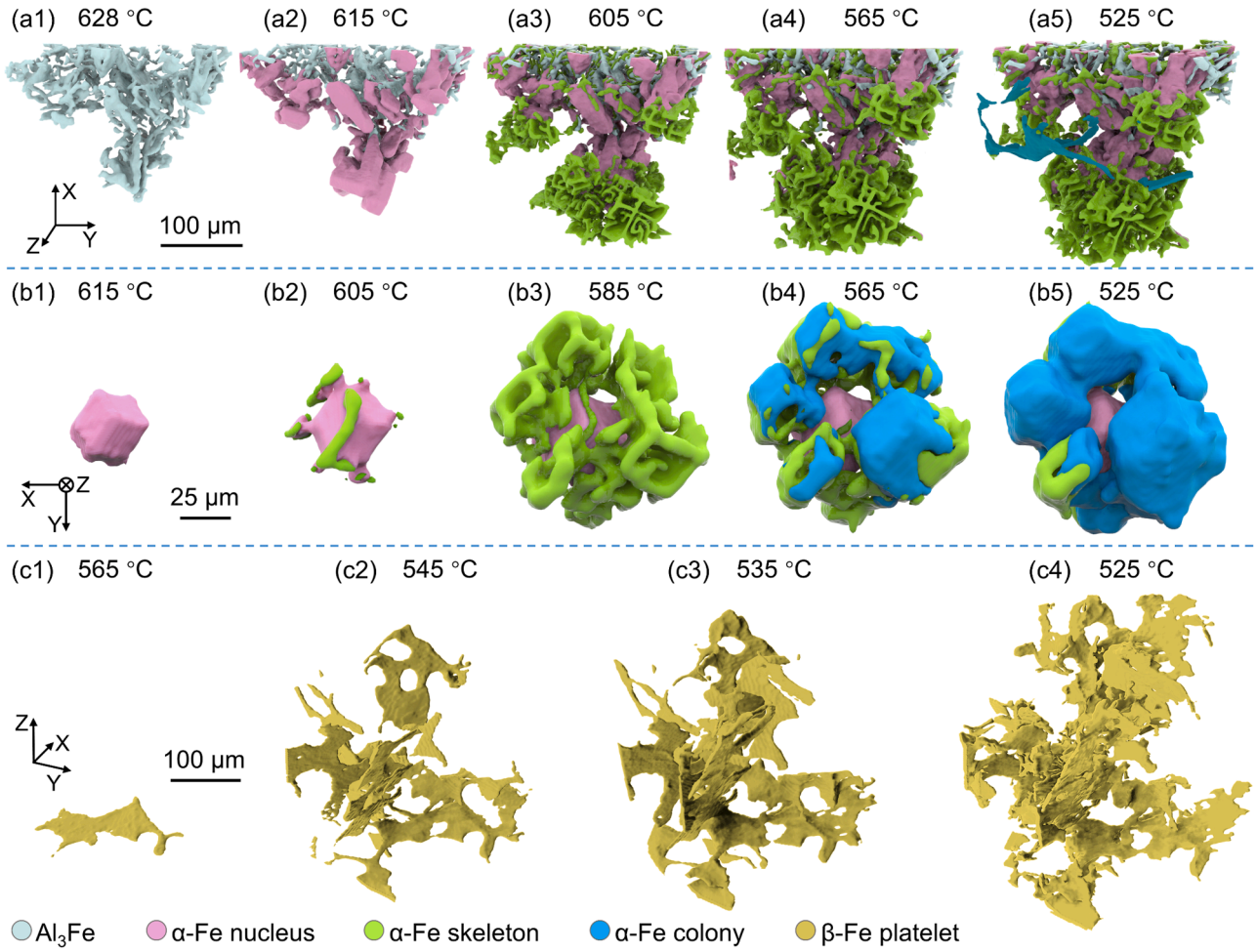

Fig. 8. The 3D morphology evolution of 3 different Fe phases in the alloy without USMP: (a1-a5) the α-Fe phase grew on top of the Al_3Fe phases; (b1-b5) the α-Fe nucleus and its growth into complex skeleton structures (see Video 4 for the nucleation and growth dynamics from different view angles for the α-Fe phases); (c1-c4) the lateral growth and branching of β-Fe plates (see Video 5 for the nucleation and growth dynamics from different view angles for the β-Fe phase).

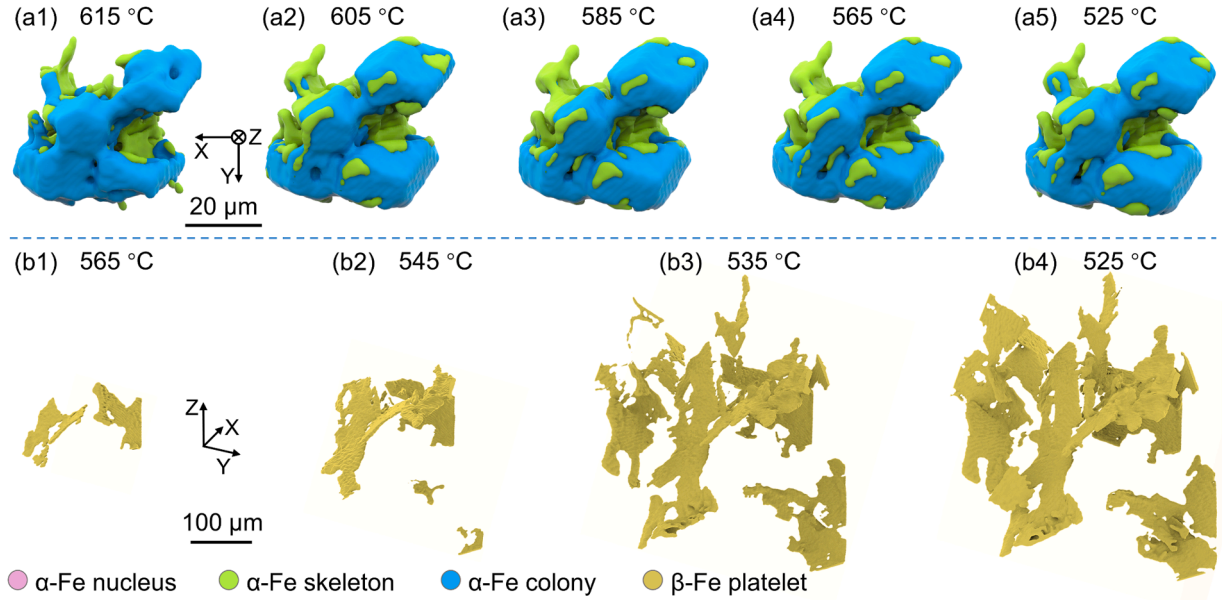

Fig. 9. The 3D morphology evolution of two different Fe phases in the alloy with USMP: (a1-a5) the growth of compact α-Fe colonies; (b1-b4) the lateral growth and branching of β-Fe phases.

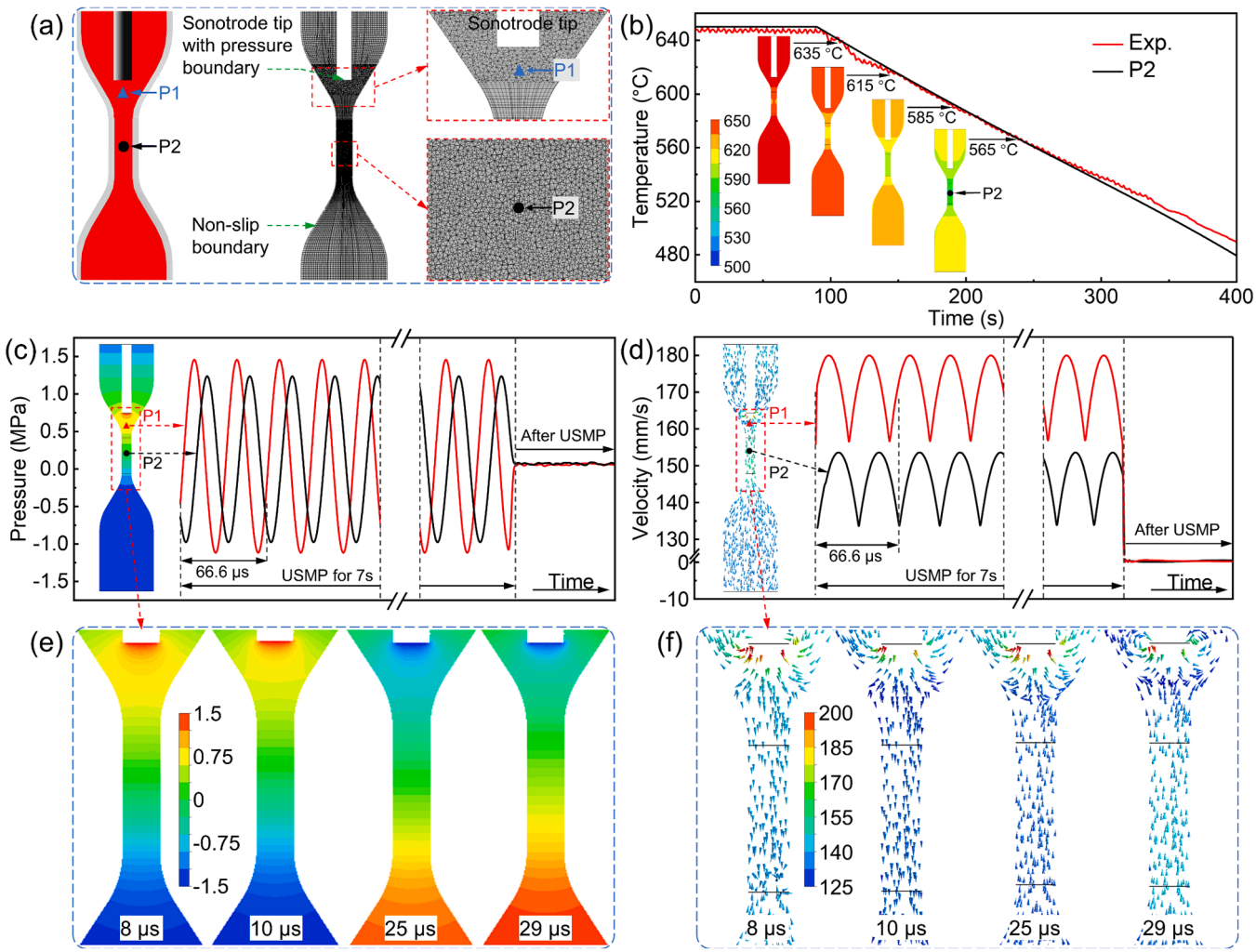

Fig. 10. (a) The computational domain and mesh structures (only showing a 2D sectional view because of the axis symmetrical nature of the model) as well as the boundary conditions. (b) Comparison of the calculated and experimentally measured temperature profile at P2 along with the temperature distribution at some critical temperature points. (c) and (d) The simulated pressure and fluid flow velocity profiles at P1 and P2 during USMP and afterwards. (e) and (f) The evolution of the pressure field and fluid flow velocity vectors in about one half of an ultrasound cycle. The data shown are those in the dotted-red rectangles of 10c & d.

to 65 KPa and 0.5 mm/s respectively, similar to natural convection in conventional solidification cases [50].

4. Discussion

4.1. Nucleation dynamics of the polygonal α-Fe nucleus

In general, the final morphology of a crystal is influenced and determined by the intrinsic crystallography characteristics (internal factors) and the surrounding environment for crystal growth (external factors) [65]. The internal factors drive the crystal growth towards a perfect crystal shape with minimum total surface free energy, whereas different external factors usually affect the crystal shape by forcing them to deviate from the equilibrium and develop into various sizes and morphologies. Therefore, the crystal growth is closely related to the growth kinetics, such as interfacial properties, solute distribution, heat and mass transfer, etc. [66,67].

The atom structures in a liquid melt consist of a large number of free atoms (atom clusters) [68,69]. Nano and micro scale segregation do exist in a free melt [70-72]. Solidification is essentially a diffusion-controlled atomic movement and rearrangement process [73, 74]. According to the phase diagram calculation and in-situ X-ray diffraction results (Fig. 3), the primary α-Al phase was formed just prior to the α-Fe phase, which consumed a certain amount of Al and expelled the solute elements (Fe, Si, and Cu) into the Al inter-dendritic region, resulting in localised solute segregation. These solute-enriched atomic clusters are prone to new crystal nucleation via the mechanism of structure and/or energy fluctuations [71,75]. In addition, some Al_3Fe phases were also formed immediately after α-Al, and they can act as the preferred substrate for the nucleation of α-Fe phases [12].

Figs. 11a1-4 show the crystallographic directions and planes that govern the growth of the α-Fe phase (a BCC - body-centred cubic structure crystal) and Figs. 11b1-4 show the actual morphology evolution of the α-Fe phase during solidification. To minimise the free energy change in nucleation, the embryonic nucleus prefers to form spherical (or near-circular) morphology [66,71]. When an embryo exceeds a critical size, it loses its stability and grows into uneven faceted surface with small perturbation and hillocks along different directions which is governed by its strong anisotropic crystalline characteristics, eventually forming a faceted morphology [71,76]. According to the Bravais-Friedel empirical law [77], the order of preferred growth orientation of crystal facets depends on the reticular density: i.e., the particular facets with lower reticular density grow faster along the stacking directions [65]. The reticular density is defined as the number of atoms (or its fraction) per unit area on a plane [78]. For the crystal with BCC structure, the reticular densities of some important crystalline faces are in the order of

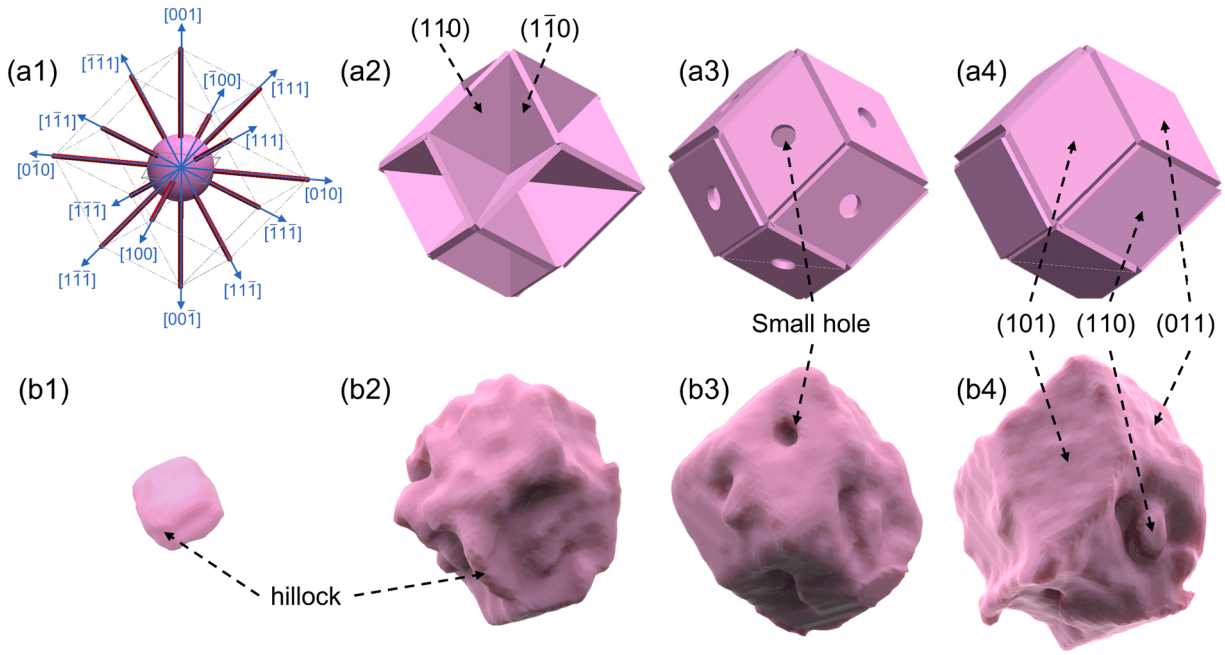

Fig. 11. (a1-a4) the crystallographic directions and planes that govern the growth dynamics of the α-Fe phases. (b1-b4) the actual morphology evolution of the α-Fe nucleus in the early stage of the solidification.

{110} > {111} > {100}. Therefore, its growth velocity should exhibit the opposite order, i.e., $V_{\{110\}} < V_{\{111\}} < V_{\{100\}}$, where $V_{\{100\}}$ is defined as the growth rate of the {100} plane along its normal direction, i.e., [100] direction [76]. As a result, the actual exposed crystal facets are the slowest-growing facets, i.e., facets (dense planes) with the highest reticular density.

Clearly, the α-Fe nuclei exhibited three distinctive stages: (1) near-circular embryo growing into hopper-shaped skeleton structures, (2) filling of interstitial space, and (3) formation of a rhombic dodecahedron. At the first stage, a spherical embryo first grew into uneven faceted surface with small perturbation and hillocks along ⟨100⟩ direction (i.e., [100], [010], [001], [$\bar{1}$00], [0$\bar{1}$0], and [00$\bar{1}$]). Then, secondary branches were formed along ⟨111⟩ direction. This was termed as "skeletal growth", and such similar growth behaviours had been also observed in the formation of the Mg_2Si phase with face-centred cubic (FCC) structure [66,79]. Subsequently, due to the strongly intrinsic faceting tendency of anisotropic crystals, these nearest branches were interconnected to form {110} facets with the lowest surface free energy, leading to the formation of skeletons with hollow hoppers (Fig. 11a2) [32,33,80]. As the solidification proceeded, the interstitial space inside the hopper was gradually filled via the deposition of atomic clusters (or some atoms) along ⟨110⟩ direction. The filling efficiency was mainly

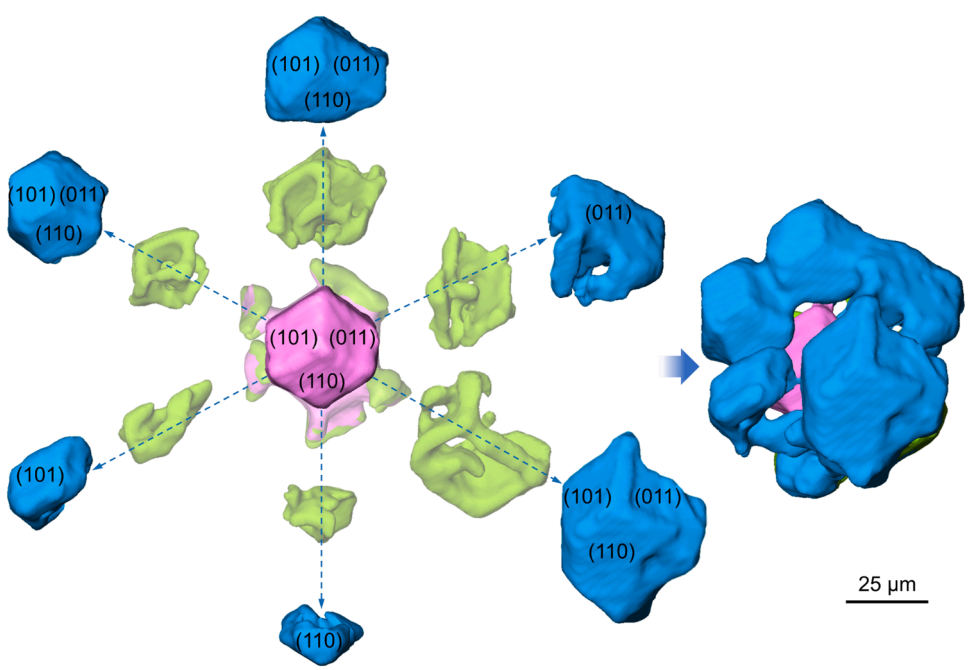

Fig. 12. (a) An exploded 3D view, showing of the growth dynamics of the α-Fe skeleton branches (light green) and colonies (blue) from the core (pink) along preferred directions.

influenced by the surrounding solute distribution and volume-diffusion [33]. At this stage, the transfer of mass was important, especially for the outer exposed {110} facets. As the solute diffusion and absorption in the central region of these facets was more difficult than that near the tips and edges whilst impurities repelled from the surface were accumulated at the solid-liquid interface [81-83], slowing down the growth rate, small voids were gradually formed on these facets (Figs. 11a3&b3). Eventually, these voids were partially filled, and the nuclei developed into rhombic dodecahedron bounded by {110} dense planes (Figs. 11a4&b4).

4.2. Co-growth dynamics of the α-Fe skeleton colonies

As solidification proceeds, multiple skeleton structures were formed from tips and edges of the core. Fig. 12 illustrates the structural evolution of typical α-Fe colonies, consisting of a nucleus and multiple skeleton branches. The growth pattern of the skeleton branches inherited that of the polygonal nuclei, i.e., growing preferentially along ⟨100⟩ and ⟨111⟩ directions and forming {110} facets driven by facet growth kinetics. EDX analyses (Fig. S3a) indicate that the α-Fe nucleus and skeleton branches have similar chemical composition in Si and Cu, but with relatively higher Fe in the nucleus. Comparison of the diffusion coefficient changes of Fe, Si and Cu in Al shows that the diffusion coefficient of Fe is approximately 1 order of magnitude lower than that of Cu and Si (Fig. S3b), resulting in much less Fe concentration in the skeleton branches (formed in the later stage of solidification) than that in the nucleus (formed at the initial stage of solidification) during solidification, whereas the concentrations of Si and Cu in the nucleus and branches are only slightly different. Such growth behaviour from tips and edges has also been observed in other anisotropic crystals grown from solutions or melts [84-90]. These facets gradually self-assembled into a series of hopper-shaped skeleton structures. Unlike the solid cores, the interior of these skeleton structures was actually filled with α-Al phases [71,91]. The interior and surrounding α-Al phases were removed to reveal more clearly the 3D morphology of the Fe phases. Subsequently, such growing process repeated in 3D space and finally developed into complicated and convoluted Chinese-script α-Fe phase colonies. Ideally, these skeleton colonies would follow the same growth behaviour as the polygonal nuclei and develop a perfect rhombic dodecahedral shape. However, due to the impediment of the already formed α-Al dendrites around them, the growth of the Fe phases was further restricted, growing into different sizes and exhibiting distorted and convoluted morphologies (see Figs. 7d and e).

4.3. Effects of USMP on the nucleation and growth of α-Al and Fe-rich phases

It is widely accepted that the refinement and homogenisation mechanisms of the solidification microstructures by USMP are due to two effects: (1) ultrasonic streaming flow enhanced thermal and solute homogenisation, (2) acoustic cavitation and bubble implosion induced structure fragmentation [19,28,37,38,42,92]. Our previous work [37,38,42,92,93] has demonstrated that USMP is capable of generating strong swirling acoustic streaming flows (up to 300 mm/s) into Al-Cu alloy melts. For example, Al_2Cu intermetallics formed in the solidification of Al-35wt%Cu were broken up and swept out of the field of view after 5 s of ultrasound application. After ultrasound process, a great number of small fragments formed and grew into equiaxed morphology [38]. Also, just 10 s of ultrasound application at an early stage of the solidification of Al-15wt%Cu was able to produce ~100 % refinement effect on α-Al dendrites compared to the case without ultrasound, resulting in 20~25 % reduction in the average grain size [42]. In this work, since the ultrasound was applied for just 7 s above the liquidus (~635 °C), there was no solid phases formed in the melt before or during USMP, meaning that no structure fragmentation occurred in the liquid state. However, the *in-situ* observations demonstrated clearly that such a short ultrasound operation time (~7 s) was sufficient to change the morphology, size and distribution of the α-Al dendrites and Fe-rich phases compared to the case without USMP. The simulation results (Fig. 10) show that the melt velocity fields induced by the oscillating ultrasonic pressure reached to 155 mm/s at P2, which is nearly 300 times higher than that after USMP (0.5 mm/s, i.e., in the natural convection state), resulting in a drastic and high-frequency convective melt stirring effect (see Fig. 10.d - the melt velocity field during USMP).

It is widely accepted that, above the cavitation threshold, the acoustic cavitation can increase local melt undercooling. In addition, the very quick oscillating acoustic pressure field (see Fig. 10c) and the strong melt perturbation (see Fig. 10d) are very effectively in homogenizing the thermal and solute distributions of the melt and therefore to reduce very effectively the solute suppressed nucleation effects for multiple component alloys as in this case [94]. It also helps to dissipate the latent heat released at the initial phase nucleation stage. The above combined effects are therefore very effective in promoting grain (or phase) nucleation rate and the initial nuclei's growth rate [13,28,95] as evidenced in Fig. 6b (for the α-Al dendrites) and Fig. 7b (for the Fe-phases). For the USMP case, although the subsequent solidification occurred without any further ultrasound applied, the enhanced grain nucleation effect has indeed resulted in much higher number of α-Al and Al_3Fe nuclei in the melt as the phase diagram calculation (Fig. 3a) and in-situ X-ray diffraction (Fig. 3c, d) indicate that the Al_3Fe phases appeared just 2–3 °C below the α-Al dendrites. However, the α-Al has much higher growth rate compared to the Al_3Fe and other Fe-phases because the Fe diffusion rate is at least 1 order of magnitude slower than that of the Al (see Fig.S3 in the Supplementary Materials). Hence, the α-Al grew much faster into dendritic structures, while the initially nucleated Fe phases remained in their "original sites", looked like to be trapped between the α-Al inter-dendritic regions. Higher number of the α-Al nuclei in the case of USMP resulted in much smaller and more frequently overlapped α-Al inter-dendritic regions. While the trapped Fe-phases have much smaller free space for continuing to grow, leading to the formation of much smaller and more compact Fe phases or Fe phase clusters [42,94]. As a result, the average size of the α-Al dendrites and the Fe-containing intermetallic phases reduced by ~5 times compared to the case without USMP (see Figs. 6 and 7).

5. Conclusion

Using synchrotron X-rays and machine-learning enabled phase segmentation strategy plus multi-physics modelling approach, we have studied under operando conditions the nucleation and co-growth dynamics of multiple Fe-rich intermetallics and their dynamic interactions with the Al dendrites of the Al5Cu1.5Fe1Si alloy in solidification with and without ultrasound. This systematic research work has produced very rich 4D (3D space + time) datasets that allow us to fully understand the dynamic interplays between the Al dendrites and multiple Fe phases and how the Fe phase evolved into complex and convoluted 3D network structures. The important findings of this research are:

1) The α-Fe phases were nucleated either from the Al_3Fe phases or directly from the liquid melt. The α-Fe embryonic nucleus had a circular morphology, it grew into uneven faceted surfaces and then gradually transformed into rhombic dodecahedron bounded by the {110} dense planes. The skeleton branched out from the dodecahedron's edges and tips, growing into 3D skeletons with α-Al inside the hoppers. Such skeleton growth process repeated in 3D space to eventually form the complex and convoluted Chinese-script clusters or colonies.
2) As solidification proceeded, the β-Fe phases nucleated directly from the residual liquid melt. They grew laterally and branched out, wrapping around the α-Al dendrite arms and eventually impinging on each other or the nearby α-Fe phases.

3) Application of high-frequency ultrasound of just 7 s in the liquid state produced oscillating ultrasonic pressure fields and melt velocity fields as high as 1.5 MPa and 150 mm/s in the melt, very effectively homogenising thermal and solute distribution of the melt, leading to a much-increased homogenous nucleation rate. As a result, the average α-Al dendrite size was decreased by ~5 times at the early stage of solidification which, in turn, further restricting the free growth of the Fe phases, reducing the Fe phases by ~5 times in terms of the average size compared to the case without ultrasound.

CRediT authorship contribution statement

Kang Xiang: Writing – review & editing, Visualization, Software, Methodology, Formal analysis. **Ling Qin:** Writing – review & editing, Visualization, Validation, Formal analysis. **Yuliang Zhao:** Writing – review & editing, Writing – original draft, Resources, Methodology, Investigation, Data curation. **Shi Huang:** Writing – review & editing, Visualization. **Wenjia Du:** Methodology, Investigation. **Elodie Boller:** Resources, Investigation. **Alexander Rack:** Resources, Investigation. **Mengnie Li:** Supervision, Software. **Jiawei Mi:** Writing – review & editing, Validation, Supervision, Resources, Project administration, Methodology, Investigation, Funding acquisition, Data curation, Conceptualization.

Declaration of Competing Interest

I declare that there is no conflict of interest among all authors concerning the submitted manuscript.

Acknowledgements

We would like to acknowledge the funding and financial supports given by the UK Engineering and Physical Science Research Council (EP/L019965/1), the National Natural Science Foundation of China (52104373) and Yunnan International Cooperation Base in Cloud Computation for Non-ferrous Metal Processing (202203AE140011). We also would like to acknowledge the synchrotron X-ray beam time awarded by ID19 beamline of the European Synchrotron Radiation Facility (proposal No. MA 3752) and beamline I12 of the Diamond Light Source (proposal No. MG27571–3); the free access to the University of Hull Supercomputer, Viper and the strong support from the technical team, in particular Mr Chris Collins. K. Xiang and S. Huang would also like to acknowledge the financial support from the University of Hull and China Scholarship Council for their PhD studies at the University of Hull.

Supplementary materials

Supplementary material associated with this article can be found, in the online version, at doi:10.1016/j.actamat.2024.120267.

References

[1] E. Aluminium, European Aluminium's Contribution to the Eu's Mid-Century Low-Carbon Roadmap, European Aluminium, Brussels, Belgium, 2019.
[2] D. Raabe, D. Ponge, P.J. Uggowitzer, M. Roscher, M. Paolantonio, C. Liu, H. Antrekowitsch, E. Kozeschnik, D. Seidmann, B. Gault, Making sustainable aluminum by recycling scrap: the science of "dirty" alloys, Prog. Mater. Sci. 128 (2022) 100947.
[3] K.N. Maung, T. Yoshida, G. Liu, C.M. Lwin, D.B. Muller, S. Hashimoto, Assessment of secondary aluminum reserves of nations, Resour. Conserv. Recycl. 126 (2017) 34–41.
[4] B. Wan, W. Chen, T. Lu, F. Liu, Z. Jiang, M. Mao, Review of solid state recycling of aluminum chips, Resour. Conserv. Recycl. 125 (2017) 37–47.
[5] S.K. Das, J.A. Green, J.G. Kaufman, D. Emadi, M. Mahfoud, Aluminum recycling—an integrated, industrywide approach, JOM 62 (2010) 23–26.
[6] J.A. Green, Aluminum Recycling and Processing for Energy Conservation and Sustainability, ASM International, 2007.
[7] K. Ganjehfard, R. Taghiabadi, M.T. Noghani, M.H. Ghoncheh, Tensile properties and hot tearing susceptibility of cast Al-Cu alloys containing excess Fe and Si, Int. J. Miner. Metallur. Mater. 28 (4) (2020) 718–728.
[8] L. Bo, H. Xiangxiang, X. Rui, Z. Yuliang, L. Yemao, X. Huaqiang, Evolution of iron-rich intermetallics and its effect on the mechanical properties of Al–Cu–Mn–Fe–Si alloys after thermal exposure and high-temperature tensile testing, J. Mater. Res. Technol. 23 (2023) 2527–2541.
[9] Y. Zhao, W. He, J. Medina, D. Song, Z. Sun, Y. Xue, G. González-Doncel, R. Fernández, Contribution of the Fe-rich phase particles to the high temperature mechanical behaviour of an Al-Cu-Fe alloy, J. Alloys Compd. 973 (2024) 172866.
[10] N.A. Belov, A.A. Aksenov, Iron in Aluminum Alloys: Impurity and Alloying Element, CRC Press, 2002.
[11] Y. Zhao, Z. Wang, C. Zhang, W. Zhang, Synchrotron X-ray tomography investigation of 3D morphologies of intermetallic phases and pores and their effect on the mechanical properties of cast Al-Cu alloys, J. Alloys Compd. 777 (2019) 1054–1065.
[12] Y. Zhao, D. Song, H. Wang, X. Li, L. Chen, Z. Sun, Z. Wang, T. Zhai, Y. Fu, Y. Wang, S. Liu, Y. Du, W. Zhang, Revealing the nucleation and growth mechanisms of Fe-rich phases in Al–Cu–Fe(-Si) alloys under the influence of Al–Ti–B, Intermetallics 146 (2022) 107584.
[13] Y. Zhao, W. He, D. Song, W. Zhang, F. Shen, B. Ma, Y. Jia, Z. Sun, Y. Fu, R. Fernández, In-situ synchrotron X-ray radiography study of primary Fe-rich phases growth in Al-Fe(Cu) alloys, Mater. Charact. 195 (2023) 112539.
[14] D. Song, Y. Zhao, Y. Jia, X. Li, Y. Fu, W. Zhang, Synergistic effects of Mn and B on iron-rich intermetallic modification of recycled Al alloy, J. Mater. Res. Technol. 24 (2023) 527–541.
[15] Y. Zhao, W. Du, B. Koe, T. Connolley, S. Irvine, P.K. Allan, C.M. Schlepütz, W. Zhang, F. Wang, D.G. Eskin, J. Mi, 3D characterisation of the Fe-rich intermetallic phases in recycled Al alloys by synchrotron X-ray microtomography and skeletonisation, Scr. Mater. 146 (2018) 321–326.
[16] L. Jiang, B. Rouxel, T. Langan, T. Dorin, Coupled segregation mechanisms of *Sc*, Zr and Mn at θ′ interfaces enhances the strength and thermal stability of Al-Cu alloys, Acta Mater. 206 (2021) 116634.
[17] T.M. Ribeiro, E. Catellan, A. Garcia, C.A. dos Santos, The effects of Cr addition on microstructure, hardness and tensile properties of as-cast Al–3.8wt.%Cu–(Cr) alloys, J. Mater. Res. Technol. 9 (3) (2020) 6620–6631.
[18] Q. Han, Ultrasonic processing of materials, Metallurg. Mater. Trans. B 46 (2015) 1603–1614.
[19] D.G. Eskin, J. Mi, Solidification Processing of Metallic Alloys Under External Fields, Springer International Publishing, 2018.
[20] G.I. Eskin, D.G. Eskin, Ultrasonic Treatment of Light Alloy Melts, CRC press, 2014.
[21] D. Eskin, I. Tzanakis, F. Wang, G. Lebon, T. Subroto, K. Pericleous, J. Mi, Fundamental studies of ultrasonic melt processing, Ultrason. Sonochem. 52 (2019) 455–467.
[22] K. Xiang, S. Huang, J. Mi, Characterisations of the Al-Mn intermetallic phases formed under pulse magnetic fields solidification, IOP Conf. Ser.: Mater. Sci. Eng. 1274 (1) (2023).
[23] H. Kotadia, M. Qian, D. Eskin, A. Das, On the microstructural refinement in commercial purity Al and Al-10 wt% Cu alloy under ultrasonication during solidification, Mater. Des. 132 (2017) 266–274.
[24] J.G. Jung, Y.H. Cho, S.D. Kim, S.B. Kim, S.H. Lee, K. Song, K. Euh, J.M. Lee, Mechanism of ultrasound-induced microstructure modification in Al-Zr alloys, Acta Mater. 199 (2020) 73–84.
[25] J.G. Jung, T.Y. Ahn, Y.H. Cho, S.H. Kim, J.M. Lee, Synergistic effect of ultrasonic melt treatment and fast cooling on the refinement of primary Si in a hypereutectic Al-Si alloy, Acta Mater. 144 (2018) 31–40.
[26] Y. Xuan, T. Liu, L. Nastac, L. Brewer, I. Levin, V. Arvikar, The influence of ultrasonic cavitation on the formation of Fe-rich intermetallics in A383 alloy, Metallurg. Mater. Trans. A 49 (2018) 3346–3357.
[27] C. Todaro, M. Easton, D. Qiu, G. Wang, D. StJohn, M. Qian, Effect of ultrasonic melt treatment on intermetallic phase formation in a manganese-modified Al-17Si-2Fe alloy, J. Mater. Process. Technol. 271 (2019) 346–356.
[28] H.R. Kotadia, M. Qian, A. Das, Microstructural modification of recycled aluminium alloys by high-intensity ultrasonication: observations from custom Al–2Si–2Mg–1.2Fe–(0.5,1.0)Mn alloys, J. Alloys Compd. 823 (2020) 153833.
[29] G. Zhong, S. Wu, H. Jiang, P. An, Effects of ultrasonic vibration on the iron-containing intermetallic compounds of high silicon aluminum alloy with 2% Fe, J. Alloys Compd. 492 (1–2) (2010) 482–487.
[30] J. Barbosa, H. Puga, J. Oliveira, S. Ribeiro, M. Prokic, Physical modification of intermetallic phases in Al–Si–Cu alloys, Mater. Chem. Phys. 148 (3) (2014) 1163–1170.
[31] S. Chankitmunkong, D.G. Eskin, C. Limmaneevichitr, Structure refinement, mechanical properties and feasibility of deformation of hypereutectic Al–Fe–Zr and Al–Ni–Zr alloys subjected to ultrasonic melt processing, Mater. Sci. Eng. A. 788 (2020) 139567.
[32] T. Gao, Y. Wu, C. Li, X. Liu, Morphologies and growth mechanisms of α-Al(FeMn)Si in Al–Si–Fe–Mn alloy, Mater. Lett. 110 (2013) 191–194.
[33] A. Bjurenstedt, D. Casari, S. Seifeddine, R.H. Mathiesen, A.K. Dahle, In-situ study of morphology and growth of primary α-Al(FeMnCr)Si intermetallics in an Al-Si alloy, Acta Mater. 130 (2017) 1–9.
[34] S. Feng, Y. Cui, E. Liotti, A. Lui, C.M. Gourlay, P.S. Grant, In-situ X-ray radiography of twinned crystal growth of primary Al13Fe4, Scr. Mater. 184 (2020) 57–62.
[35] B. Kim, S. Lee, S. Lee, H. Yasuda, Real-time radiographic observation of solidification behavior of Al–Si–Cu casting alloys with the variation of iron content, Mater. Trans. 53 (2) (2012) 374–379.

[36] D.H. Bilderback, P. Elleaume, E. Weckert, Review of third and next generation synchrotron light sources, J. Phys. B: Atomic Mol. Opt. Phys. 38 (9) (2005) S773.
[37] B. Wang, D. Tan, T.L. Lee, J.C. Khong, F. Wang, D. Eskin, T. Connolley, K. Fezzaa, J. Mi, Ultrafast synchrotron X-ray imaging studies of microstructure fragmentation in solidification under ultrasound, Acta Mater. 144 (2018) 505–515.
[38] F. Wang, D. Eskin, J. Mi, C. Wang, B. Koe, A. King, C. Reinhard, T. Connolley, A synchrotron X-radiography study of the fragmentation and refinement of primary intermetallic particles in an Al-35 Cu alloy induced by ultrasonic melt processing, Acta Mater. 141 (2017) 142–153.
[39] W. Xu, I. Tzanakis, P. Srirangam, W. Mirihanage, D. Eskin, A. Bodey, P. Lee, Synchrotron quantification of ultrasound cavitation and bubble dynamics in Al–10Cu melts, Ultrason. Sonochem. 31 (2016) 355–361.
[40] S. Wang, Z. Guo, J. Kang, M. Zou, X. Li, A. Zhang, W. Du, W. Zhang, T.L. Lee, S. Xiong, J. Mi, 3D phase field modeling of multi-dendrites evolution in solidification and validation by synchrotron X-ray tomography, Materials 14 (3) (2021).
[41] Z. Li, L. Qin, B. Guo, J. Yuan, Z. Zhang, W. Li, J. Mi, Characterization of the convoluted 3D intermetallic phases in a recycled Al alloy by synchrotron X-ray tomography and machine learning, Acta Metall. Sin. (Engl. Lett.) 35 (1) (2021) 115–123.
[42] Z. Zhang, C. Wang, B. Koe, C.M. Schlepütz, S. Irvine, J. Mi, Synchrotron X-ray imaging and ultrafast tomography in situ study of the fragmentation and growth dynamics of dendritic microstructures in solidification under ultrasound, Acta Mater. 209 (2021) 116796.
[43] Z. Zhang, J.C. Khong, B. Koe, S. Luo, S. Huang, L. Qin, S. Cipiccia, D. Batey, A. J. Bodey, C. Rau, Y.L. Chiu, Z. Zhang, J.-C. Gebelin, N. Green, J. Mi, Multiscale characterization of the 3D network structure of metal carbides in a Ni superalloy by synchrotron X-ray microtomography and ptychography, Scr. Mater. 193 (2021) 71–76.
[44] Z. Song, O.V. Magdysyuk, T. Sparks, Y.-L. Chiu, B. Cai, Revealing growth mechanisms of faceted Al2Cu intermetallic compounds via high-speed Synchrotron X-ray tomography, Acta Mater. 231 (2022) 117903.
[45] S. Feng, Z. Jin, W. Du, I. Han, A. Lui, X. Zhou, P.R. Shearing, P.S. Grant, E. Liotti, The mechanism of Fe-rich intermetallic compound formation and growth on inoculants revealed by electron backscattered diffraction and X-ray imaging, Mater. Des. 232 (2023) 112110.
[46] Z. Song, E. Boller, A. Rack, P.D. Lee, B. Cai, Magnetic field-assisted solidification of W319 Al alloy qualified by high-speed synchrotron tomography, J. Alloys Compd. 938 (2023) 168691.
[47] S.Y. Sun, Q.D. Hu, W.Q. Lu, Z.Y. Ding, M.Q. Xu, M.X. Xia, J.G. Li, In situ study on the growth behavior of primary Al-Ni phase in solidifying Al-Ni Alloy by synchrotron radiography, Acta Metall. Sin. (Engl. Lett.) 31 (6) (2018) 668–672.
[48] E. Liotti, C. Arteta, A. Zisserman, A. Lui, V. Lempitsky, P.S. Grant, Crystal nucleation in metallic alloys using x-ray radiography and machine learning, Sci. Adv. 4 (4) (2018) eaar4004.
[49] Z. Xuan, F. Mao, Z. Cao, T. Wang, L. Zou, In situ observation on the solidification of Sn-10Cu hyperperitectic alloy under direct current field by synchrotron microradiography, J. Alloys Compd. 721 (2017) 126–133.
[50] L. Qin, W. Du, S. Cipiccia, A.J. Bodey, C. Rau, J. Mi, Synchrotron X-ray operando study and multiphysics modelling of the solidification dynamics of intermetallic phases under electromagnetic pulses, Acta Mater. 265 (2024) 119593.
[51] C. Puncreobutr, A.B. Phillion, J.L. Fife, P. Rockett, A.P. Horsfield, P.D. Lee, In situ quantification of the nucleation and growth of Fe-rich intermetallics during Al alloy solidification, Acta Mater. 79 (2014) 292–303.
[52] Z. Song, O.V. Magdysyuk, L. Tang, T. Sparks, B. Cai, Growth dynamics of faceted Al13Fe4 intermetallic revealed by high-speed synchrotron X-ray quantification, J. Alloys Compd. 861 (2021) 158604.
[53] S. Feng, E. Liotti, A. Lui, M.D. Wilson, T. Connolley, R.H. Mathiesen, P.S. Grant, In-situ X-ray radiography of primary Fe-rich intermetallic compound formation, Acta Mater. 196 (2020) 759–769.
[54] N. Zhang, Q. Hu, Z. Ding, W. Lu, F. Yang, J. Li, 3D morphological evolution and growth mechanism of proeutectic FeAl3 phases formed at Al/Fe interface under different cooling rates, J. Mater. Sci. Technol. 116 (2022) 83–93.
[55] B. Cai, A. Kao, P.D. Lee, E. Boller, H. Basevi, A.B. Phillion, A. Leonardis, K. Pericleous, Growth of β intermetallic in an Al-Cu-Si alloy during directional solidification via machine learned 4D quantification, Scr. Mater. 165 (2019) 29–33.
[56] S. Terzi, J.A. Taylor, Y.H. Cho, L. Salvo, M. Suéry, E. Boller, A.K. Dahle, In situ study of nucleation and growth of the irregular α-Al/β-Al5FeSi eutectic by 3-D synchrotron X-ray microtomography, Acta Mater. 58 (16) (2010) 5370–5380.
[57] T. Manuwong, W. Zhang, P.L. Kazinczi, A.J. Bodey, C. Rau, J. Mi, Solidification of Al alloys under electromagnetic pulses and characterization of the 3D microstructures using synchrotron X-ray tomography, Metallurg. Mater. Trans. A 46 (7) (2015) 2908–2915.
[58] K. Xiang, S. Huang, H. Song, V. Bazhenov, V. Bellucci, S. Birnsteinova, R. de Wijn, J.C. Koliyadu, F.H. Koua, A. Round, E. Round, A. Sarma, T. Sato, M. Sikorski, Y. Zhang, E.M. Asimakopoulou, P. PVillanueva-Perez, K. Porfyrakis, I. Tzanakis, D. G. Eskin, N. Grobert, A. Mancuso, R. Bean, P. Vagovic, J. Mi, arXiv preprint, 2023.
[59] A. Mirone, E. Brun, E. Gouillart, P. Tafforeau, J. Kieffer, The PyHST2 hybrid distributed code for high speed tomographic reconstruction with iterative reconstruction and a priori knowledge capabilities, Nucl. Instrum. Meth. B 324 (2014) 41–48.
[60] C.A. Schneider, W.S. Rasband, K.W. Eliceiri, NIH Image to ImageJ: 25 years of image analysis, Nat. Methods 9 (7) (2012) 671–675.
[61] I. Arganda-Carreras, V. Kaynig, C. Rueden, K.W. Eliceiri, J. Schindelin, A. Cardona, H.Sebastian Seung, Trainable Weka Segmentation: a machine learning tool for microscopy pixel classification, Bioinformatics. 33 (15) (2017) 2424–2426.
[62] R. Dougherty, K.-H. Kunzelmann, Computing local thickness of 3D structures with ImageJ, Microsc. Microanal. 13 (S02) (2007) 1678–1679.
[63] N. Saunders, U. Guo, X. Li, A. Miodownik, J.-P. Schillé, Using JMatPro to model materials properties and behavior, JOM 55 (12) (2003) 60–65.
[64] J. Wang, P. Lee, R. Hamilton, M. Li, J. Allison, The kinetics of Fe-rich intermetallic formation in aluminium alloys: in situ observation, Scr. Mater. 60 (7) (2009) 516–519.
[65] I. Sunagawa, Crystals: Growth, Morphology, & Perfection, Cambridge University Press, 2007.
[66] C. Li, Y.Y. Wu, H. Li, X.F. Liu, Morphological evolution and growth mechanism of primary Mg2Si phase in Al–Mg2Si alloys, Acta Mater. 59 (3) (2011) 1058–1067.
[67] G. Liu, K. Chen, H. Zhou, J. Tian, C. Pereira, J. Ferreira, Fast shape evolution of TiN microcrystals in combustion synthesis, Cryst. Growth Des. 6 (10) (2006) 2404–2411.
[68] S. Huang, K. Xiang, J. Mi, Recent advances in synchrotron X-ray studies of the atomic structures of metal alloys in liquid state, J. Mater. Sci. Technol. 203 (2024) 180–200.
[69] S. Luo, J.C. Khong, S. Huang, G. Yang, J. Mi, Revealing in situ stress-induced short- and medium-range atomic structure evolution in a multicomponent metallic glassy alloy, Acta Mater. 272 (2024) 119917.
[70] S. Huang, S. Luo, L. Qin, D. Shu, B. Sun, A.J.G. Lunt, A.M. Korsunsky, J. Mi, 3D local atomic structure evolution in a solidifying Al-0.4Sc dilute alloy melt revealed in operando by synchrotron X-ray total scattering and modelling, Scr. Mater. 211 (2022) 114484.
[71] X. Zhu, P. Blake, S. Ji, The formation mechanism of Al6(Fe, Mn) in die-cast Al–Mg alloys, CrystEngComm. 20 (27) (2018) 3839–3848.
[72] L. Song, X. Tian, Y. Yang, J. Qin, H. Li, X. Lin, Probing the microstructure in pure Al & Cu melts: theory meets experiment, Front. Chem. 8 (2020) 607.
[73] T. Zheng, P. Shi, Z. Shen, B. Zhou, W. Lin, X. Liang, W. Liu, X. Chen, Y. Zhong, H. Wang, Diffusion-controlled mechanical property-enhancement of Al-20wt.% Si ribbon annealed under high static magnetic fields, from the microscale to the atomic scale, Mater. Des. 188 (2020) 108476.
[74] Y. Zhou, Solidification Behaviour of Fe-rich intermetallic Compounds in Aluminium Alloys, Brunel University London, 2018.
[75] W.C. Yang, F. Gao, S.X. Ji, Formation and sedimentation of Fe-rich intermetallics in Al-Si-Cu-Fe alloy, Trans. Nonferrous Metals Soc. China 25 (5) (2015) 1704–1714.
[76] V. Ankudinov, P.K. Galenko, Growth of different faces in a body centered cubic lattice: a case of the phase-field-crystal modeling, J. Cryst. Growth 539 (2020) 125608.
[77] J.D.H. Donnay, D. Harker, A new law of crystal morphology extending the law of Bravais, Am. Mineralogist: J. Earth Planetary Mater. 22 (5) (1937) 446–467.
[78] G. Chadwick, A hard-sphere model of crystal growth, Metal Sci. J. 1 (1) (1967) 132–139.
[79] Q.D. Qin, Y.G. Zhao, W. Zhou, P.J. Cong, Effect of phosphorus on microstructure and growth manner of primary Mg2Si crystal in Mg2Si/Al composite, Mater. Sci. Eng. A. 447 (1–2) (2007) 186–191.
[80] A. Fabrizi, G. Timelli, The influence of cooling rate and Fe/Cr content on the evolution of Fe-rich compounds in a secondary Al-Si-Cu diecasting alloy, in: IOP Conference Series: Materials Science and Engineering, IOP Publishing, 2016 012017.
[81] L. Li, Z. Zhao, Y. Zuo, Q. Zhu, J. Cui, Effect of a high magnetic field on the morphological and crystallographic features of primary Al6Mn phase formed during solidification process, J. Mater. Res. 28 (12) (2013) 1567–1573.
[82] C.L. Xu, H.Y. Wang, C. Liu, Q.C. Jiang, Growth of octahedral primary silicon in cast hypereutectic Al–Si alloys, J. Cryst. Growth 291 (2) (2006) 540–547.
[83] A. Chernov, Stability of faceted shapes, J. Cryst. Growth 24 (1974) 11–31.
[84] Y. Li, H. Lin, W. Zhou, L. Sun, D. Samanta, C.A. Mirkin, Corner-, edge-, and facet-controlled growth of nanocrystals, Sci. Adv. 7 (3) (2021).
[85] R.Y. Wang, W.H. Li, L.M. Hogan, Faceted growth of silicon crystals in Al-Si alloys, Metall. Mater. Trans. A 28 (5) (1997) 1233–1243.
[86] R.Y. Wang, W.H. Lu, L.M. Hogan, Growth morphology of primary silicon in cast Al-Si alloys and the mechanism of concentric growth, J. Cryst. Growth 207 (1–2) (1999) 43–54.
[87] L. Huang, W. Zhang, P. Li, Y. Song, H. Sheng, Y. Du, Y.-G. Wang, Y. Wu, X. Hong, Y. Ding, X. Yuan, M. Zhu, Exposing Cu-Rich {110} Active Facets in PtCu nanostars for boosting electrochemical performance toward multiple liquid fuels electrooxidation, Nano Res. 12 (5) (2019) 1147–1153.
[88] L. Hu, H. Lu, X. Ma, X. Chen, Heterogeneous nucleation on surfaces of the three-dimensional cylindrical substrate, J. Cryst. Growth 575 (2021) 126340.
[89] N.H. Fletcher, Size effect in heterogeneous nucleation, J. Chem. Phys. 29 (3) (1958) 572–576.
[90] D. Turnbull, Kinetics of heterogeneous nucleation, J. Chem. Phys. 18 (2) (1950) 198–203.
[91] O. Trudonoshyn, O. Prach, A. Slyudova, V. Lisovskii, Structure formation and multistep nucleation in CASTING Al-Mg-Si alloys, Int. J. Cast Metals Res. 33 (4–5) (2020) 184–193.
[92] F. Wang, D. Eskin, J. Mi, T. Connolley, J. Lindsay, M. Mounib, A refining mechanism of primary Al3Ti intermetallic particles by ultrasonic treatment in the liquid state, Acta Mater. 116 (2016) 354–363.

[93] H. Huang, L. Qin, H. Tang, D. Shu, W. Yan, B. Sun, J. Mi, Ultrasound cavitation induced nucleation in metal solidification: an analytical model and validation by real-time experiments, Ultrason. Sonochem. 80 (2021) 105832.

[94] D. Shu, B. Sun, J. Mi, P.S. Grant, A quantitative study of solute diffusion field effects on heterogeneous nucleation and the grain size of alloys, Acta Mater. 59 (5) (2011) 2135–2144.

[95] X. Chavanne, S. Balibar, F. Caupin, Acoustic crystallization and heterogeneous nucleation, Phys. Rev. Lett. 86 (24) (2001) 5506–5509.